Supplementary Materials for

Glass-like Thermal Conductivity and Phonon Transport Mechanism in Disordered crystals

Guoliang Ren[1], Junwei Che[2], Hanchao Zhang[3], Yali Yu[4], Wei Hao[5], Yinchun Shi[1], Fan Yang[3*], Xiaofeng Zhao[1*]

[1]Shanghai Key Laboratory of High Temperature Materials and Precision Forming, School of Materials Science and Engineering, Shanghai Jiao Tong University, Shanghai, 200240 China.

[2]School of Science, Xi'an University of Science and Technology, Xi'an, 710054, China.

[3]School of Mechanical Engineering, Shanghai Jiao Tong University, Shanghai, 200240, China.

[4]State Key Laboratory of New Ceramics and Fine Processing, School of Materials Science and Engineering, Tsinghua University, Beijing, 100084, China.

[5]College of Engineering, Zhejiang Normal University, Jinhua, 321004, China.

*Corresponding authors. Email: fanyang_0123@sjtu.edu.cn; xiaofengzhao@sjtu.edu.cn;

1. Details for MD, BTE and DFT calculations

Classic molecular dynamic simulation

All molecular dynamic (MD) simulations were performed by using the large-scale atomic/molecular massively parallel simulator (LAMMPS) package [1]. Since rare-earth tantalates are ionic crystals, the interatomic interactions in the MC/MD simulations were described using the Born model based on the rigid body, which is expressed as follows:

$$E_{i,j} = A_{ij}\exp\left(-\frac{r_{ij}}{\rho_{ij}}\right) - \frac{C_{ij}}{r_{ij}^{6}} + \frac{1}{4\pi\varepsilon_0}\frac{q_i q_j}{r_{ij}} \quad \text{* MERGEFORMAT (1)}$$

where the subscripts i and j denote the ionic pair between the i-th and the j-th atom, r is the interatomic distance and q is the atomic charge. The parameters A_{ij}, ρ_{ij}, and C_{ij} are listed in Table S1. The first term represents the long-range Coulomb interaction, and the remaining two terms represent the short-range repulsion, and ε_0 is the vacuum permittivity. The Ewald approximation with an accuracy of 1.0e−6 was employed to calculate the long-range Coulomb potential.

The lattice constant of the defect fluorite structure of RE_3TaO_7 was initially set at 5.192 Å in a simulation cell, which is oriented with [100], [010], and [001] directions aligned respectively with x, y, and z axes. The initial structures were obtained by randomly injecting Y, Dy, Er, Ho, Yb, and Ta atoms at cationic sites according to stoichiometric ratios. The atom distribution was optimized by performing Monte Carlo (MC) site-occupancy swaps between pairs of sites under the calculated temperature respectively. The acceptance of each MC swap conforms to the Metropolis criterion [2]; that is, if the system energy following the swap attempt, $i + 1$, $E(i + 1)$, is lower than that following the previous successful swap, $E(i)$, the MC swap is accepted. Otherwise, it is accepted with a probability of [3]:

$$P = e^{\frac{E(i+1)-E(i)}{k_B T}} \quad \text{* MERGEFORMAT (2)}$$

Where T is absolute temperature. If a uniformly generated random number in the range of (0,1), R, is lower than / equal to P, the MC swap is accepted. Otherwise, it is rejected. The MC steps are interchanged with MD relaxations to efficiently converge site occupancy and atomic displacements.

According to the Green-Kubo (GK) formula, the κ of bulk samples were calculated using equilibrium molecular dynamic (EMD) simulation based on the fluctuation dissipation theory [4]:

$$\kappa = \frac{V}{3k_B T^2}\int_0^\infty \left\langle \mathbf{J}(0)\cdot\mathbf{J}(t)\right\rangle dt \qquad \backslash^* \text{ MERGEFORMAT (3)}$$

where V is the volume of the simulation cell. $\left\langle \mathbf{J}(0)\cdot\mathbf{J}(t)\right\rangle$ is the heat current autocorrelation function (HCACF). The EMD approach can eliminate the effect of the cell size on the simulation results so that the inherent κ can be obtained. The heat current **J** was calculated using the following expression [5]:

$$\mathbf{J} = \frac{1}{V}\left[\sum_i r_i\left(\frac{1}{2}m_i v_i + U_i\right)\mathbf{v}_i + \sum_i\sum_j\left(\frac{\partial U_j}{\partial r_i}\cdot\mathbf{v}_j\right)\mathbf{r}_{ij}\right] \backslash^* \text{ MERGEFORMAT (4)}$$

where m_i, v_i, U_i, $\mathbf{v}_i$, and $\mathbf{r}_i$ are the mass, velocity, potential energy, virial force, and position of the i-th atom, respectively. For each sample, 10 independent calculations were performed to calculate the average κ and evaluate the corresponding error. Unless otherwise specified, the average κ values presents below were averaged over 10 calculations.

The phonon dispersion relationship was calculated using the phonon spectral energy density (SED) [6]. This method directly projects the trajectories of atoms onto the vibrational modes to determine the distribution of the vibrational energy in the wavevector-frequency space:

$$\phi(\mathbf{q},\omega_\lambda) = \frac{1}{4\pi N_s \tau_0}\sum_\alpha\sum_b^B m_b\left|\int_0^{\tau_0}\sum_{n_{x,y,z}}^{N_s}\dot{u}_\alpha\begin{pmatrix}n_{x,y,z}\\ b\end{pmatrix};t\times\exp\left[i\mathbf{q}\cdot\mathbf{r}\begin{pmatrix}n_{x,y,z}\\ 0\end{pmatrix}-i\omega t\right]dt\right|^2 \backslash^*$$

MERGEFORMAT (5)

where **q**, ω, N_s and τ_0 are wave vector, frequency of phonon mode, the total number of unit cells and integration time. $\dot{u}_\alpha\begin{pmatrix}n_{x,y,z}\\ b\end{pmatrix};t$ is the displacement in the α direction of atom b with mass m_b inside unit cell $n_{x,y,z}$. **r** is the equilibrium position of each unit cell. In this work, 150000 trajectories were calculated in the microcanonical ensemble (NVE) for each sample.

Boltzmann transport equation

The κ of RE_3TaO_7 were also investigated based on Boltzmann transport equation (BTE) with relaxation time approximation (RTA) using the ALAMODE package [7] with the Buckingham potential. The second- and third-order interatomic force constants (IFCs) were obtained from the ALM code which is distributed with ALAMODE. The forces required to obtain IFCs were computed by the LAMMPS code. The RTA to calculate the κ_{BTE} was applied using [8]:

$$\kappa_{\mathrm{BTE}}=\frac{4\pi}{3}\frac{1}{(2\pi)^3}\sum_{\lambda}\int\frac{\hbar^2\omega^2(\mathbf{q},\lambda)}{k_BT^2}\frac{e^{\frac{\hbar\omega(\mathbf{k},\lambda)}{k_BT}}}{\left(e^{\frac{\hbar\omega(\mathbf{q},\lambda)}{k_BT}}-1\right)}v^2(\mathbf{q},\lambda)\tau(\mathbf{q},\lambda)\lambda^2 d\lambda \backslash *$$

MERGEFORMAT (6)

where $\omega(\mathbf{q},\lambda)$, $v(\mathbf{q},\lambda)$ and $\tau(\mathbf{q},\lambda)$ are the frequency, group velocity and lifetime of the phonon mode $(\mathbf{q},\lambda)$, respectively, with $\mathbf{q}$ and λ representing phonon wave vector and phonon branches.

Density functional theory (DFT) calculation

The crystal orbital Hamilton population (COHP) analysis was employed to evaluate the strength of the bonds [9,10]. The COHP analysis is a technique for partitioning the band structure energy into bonding, nonbonding, and antibonding contributions using localized atomic basis sets [9]. In analogy to the density of states (DOS), for which the energy integration up to the Fermi energy gives the number of electrons, the energy integration of all COHP for a pair of atoms up to the Fermi energy (ICOHP) can imply the bond strength [11]. All the COHP calculations were performed by the LOBSTER code [12] with the tetrahedron method.

As another method for evaluating a bond strength, the force constant between metal atoms and O atom was evaluated from the phonon calculations by self-consistent density functional perturbation theory (DFPT) in the linear response approach [13] with Phonopy code [14]. The force constant is described as a 3×3 matrix, the trace of the force constant matrix, which is scalar quantity, can be considered as the force constant F_{ij} between atoms i and j.

Based on the integrated COHP (ICOHP) analysis and force constant calculations, the strength of bonds in materials can be approximated. ICOHP analysis has been applied to measure the bond strength of various materials [10,15,16]. The force constant, as another physical quantity that relates to the strength of chemical bonds, is gradually being extended to the

analysis of bond nature of solids [17,18] and interfaces [19]. However, special care needs to be taken that ICOHP mainly measures the covalent strength part of the chemical bond, while the force constant describes the behavior of the energy potential change when the bond deviates slightly from the equilibrium scale [15].

2. Additional results from XRD and SEM

Phase and crystal structure

The experimental and Rietveld refined XRD patterns of the sintered RE_3TaO_7 specimens are shown in Fig. S1. Here the XRD diffraction peaks correspond to (111), (200), (220), (311), (222), (400), (331) and (420) in the 2-Theta range from 10º to 90º. All sintered specimens have profile residual (R_p) and weighted profile residual (R_{wp}) of less than 5%, indicating that the specimens are pure single-phase defective fluorite structures. The refined crystallographic data of representative compounds are given in Table S3. Also, the refined space group and unit cell parameters are given in Table S1. Compared with low-entropy $RETaO_7$ ($\Delta S = 0.56k_B$), the XRD peaks of the medium- and high-entropy ($\Delta S > 1.0k_B$) components integrally shift to lower 2-Theta, corresponding to bigger lattice constants shown in Table S1. This can be attributed to the fact that the interplanar spacing in high-entropy components increases as the ionic radius of trivalent cation (the radii of Y^{3+}, Dy^{3+}, Er^{3+}, Ho^{3+}, in eight-fold coordination are 1.019Å, 1.027Å, 1.004Å, 1.015Å).

Microstructure and mechanical properties

It can be seen in Fig. S2 that all sintered samples are dense with clear grain boundary. Additionally, the measured relative densities (ρ/ρ_0) of all sintered RE_3TaO_7 specimens shown in Table S4 are above 90%, indicating that almost completely dense specimens were obtained. The measured average grain size (~2 μm) and mechanical properties of all sintered samples are also listed in Table S4. Obviously, the Young's modulus of all RE_3TaO_7 specimens are lower than those of the classical YSZ and $La_2Zr_2O_7$, suggesting that RE_3TaO_7 compositions exhibit outstanding stress tolerance. The compositional uniformity of all sintered specimens was characterized by surface EDS mapping. As show in Fig.2, all the elements distribute

homogenously and no elements segregation can be found in all samples. Therefore, the XRD patterns, SEM image, and EDS mapping unanimously confirm that single-phase defective fluorite RE_3TaO_7 ceramics have been successfully prepared.

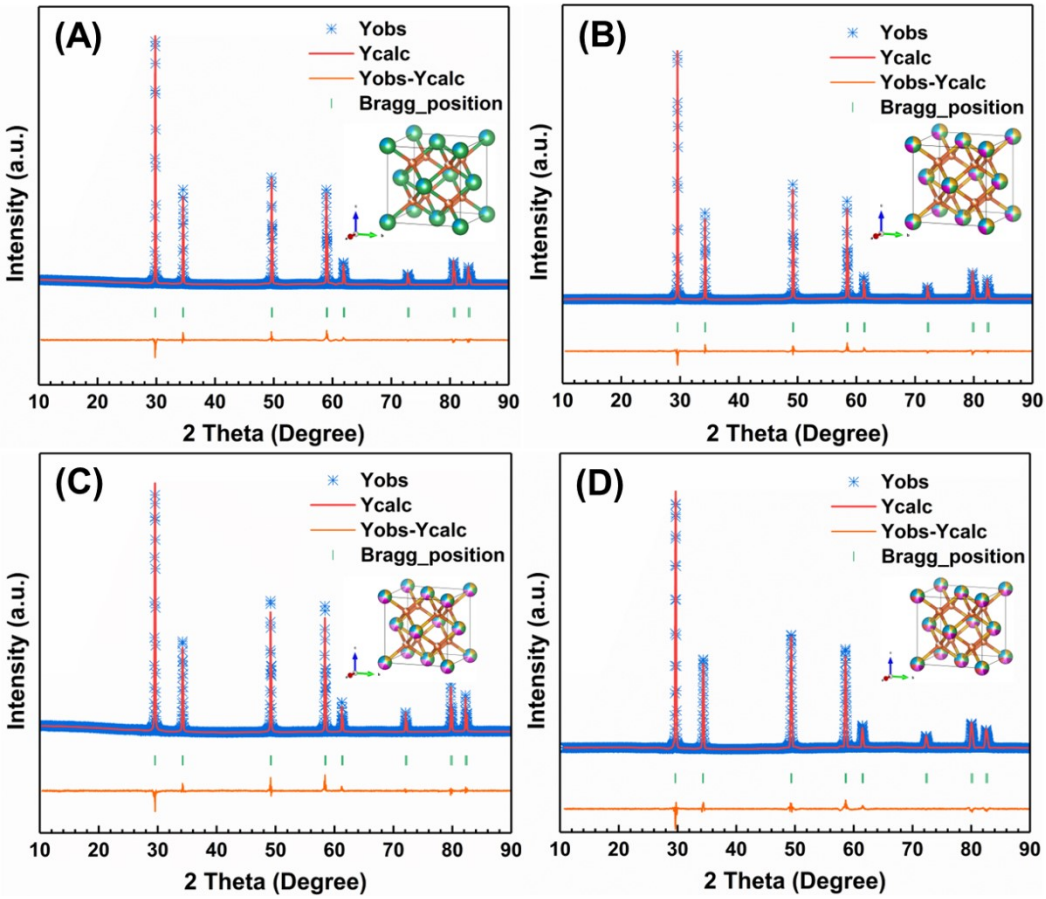

Fig.S1 XRD Rietveld refinements for the fluorite cell performed for (A) $1RETaO_7$, (B) $3RETaO_7$, (C) $4RETaO_7$, and (D) $5RETaO_7$. The insets show their crystal structure, respectively.

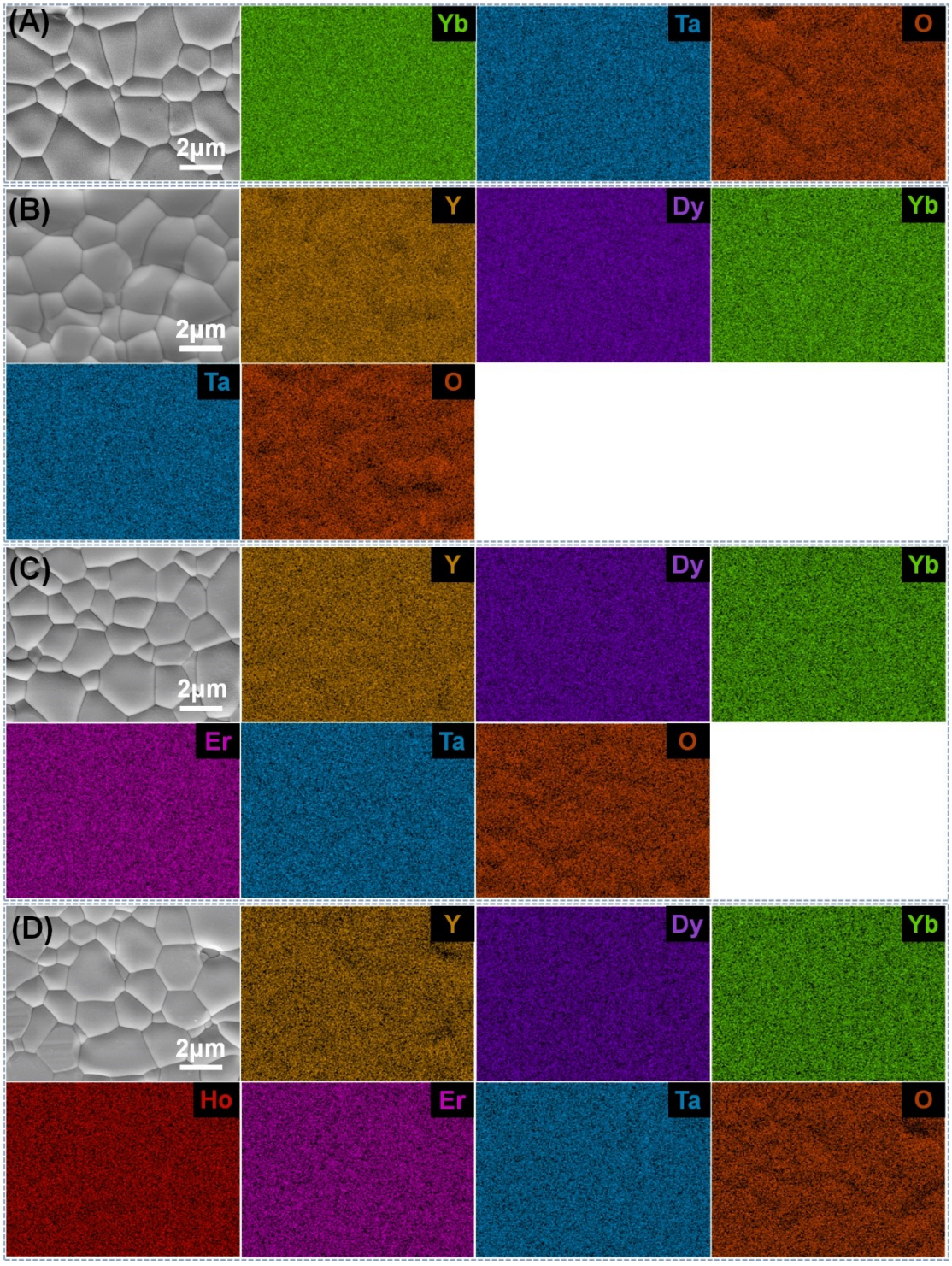

Fig. S2 The SEM images and EDS mappings of (A) $1RETaO_7$, (B) $3RETaO_7$, (C) $4RETaO_7$, and (D) $5RETaO_7$.

Table S1. Potential parameters for RE_3TaO_7 used in this study [20-22].

Species	A (eV)	ρ(Å)	C (eV·Å^6)
O–O	9547.96	0.2192	32.00
O–Ta	1315.57	0.3690	0.00
O–Y	1766.40	0.33849	19.43
O–Dy	1767.64	0.3376	10.94
O–Er	1678.21	0.33781	10.81
O–Ho	1726.29	0.33776	10.72
O–Yb	1649.80	0.3386	16.57

* For atomic pairs not listed in the table, only the Columbic term is included. (i.e. A=C=0).

Table S2. Measured and calculated unit cell parameters for the sintered RE_3TaO_7 systems. Here, the calculated lattice constants of the RE_3TaO_7 systems were obtained based on the Buckingham potential.

Composition	Abbreviation	ΔS	Space group	*a* (Å)			R_p	R_{wp}
				Exp.	Cal.	Error		
Yb_3TaO_7	1RETaO$_7$	0.56 k_B	$Fm\bar{3}m$	5.192	5.226	0.65%	1.06	1.86
$(Y_{1/3}Yb_{1/3}Dy_{1/3})_3TaO_7$	3RETaO$_7$	1.39 k_B	$Fm\bar{3}m$	5.236	5.272	0.69%	1.17	1.90
$(Y_{1/4}Yb_{1/4}Dy_{1/4}Er_{1/4})_3TaO_7$	4RETaO$_7$	1.60 k_B	$Fm\bar{3}m$	5.239	5.288	0.94%	1.10	1.78
$(Y_{1/5}Yb_{1/5}Dy_{1/5}Er_{1/5}Ho_{1/5})_3TaO_7$	5RETaO$_7$	1.77 k_B	$Fm\bar{3}m$	5.224	5.261	0.71%	1.18	1.91

Table S3. Crystallographic Data for Disordered Defect Fluorite RE_3TaO_7.

atom	site	*x*	*y*	*z*	*U*(Å^2)	occ.
1RETaO$_7$ (Yb$_3$TaO$_7$) Defect Fluorite (space group: $Fm\bar{3}m$)						
Yb	4a	0	0	0	0.003	0.750
Ta	4a	0	0	0	0.003	0.250
O	8c	0.250	0.250	0.250	0.023	0.868
3RETaO$_7$ ((Y$_{1/3}$Dy$_{1/3}$Yb$_{1/3}$)$_3$TaO$_7$) Defect Fluorite (space group: $Fm\bar{3}m$)						
Y	4a	0	0	0	0.001	0.250
Dy	4a	0	0	0	0.001	0.250
Yb	4a	0	0	0	0.001	0.250
Ta	4a	0	0	0	0.001	0.250
O	8c	0.250	0.250	0.250	0.003	0.871
4RETaO$_7$ ((Y$_{1/4}$Dy$_{1/4}$Er$_{1/4}$Yb$_{1/4}$)$_3$TaO$_7$) Defect Fluorite (space group: $Fm\bar{3}m$)						
Y	4a	0	0	0	0.001	0.188
Dy	4a	0	0	0	0.001	0.188
Er	4a	0	0	0	0.001	0.188
Yb	4a	0	0	0	0.001	0.188
Ta	4a	0	0	0	0.001	0.250
O	8c	0.250	0.250	0.250	0.023	0.870
5RETaO$_7$ ((Y$_{1/5}$Dy$_{1/5}$Ho$_{1/5}$Er$_{1/5}$Yb$_{1/5}$)$_3$TaO$_7$) Defect Fluorite (space group: $Fm\bar{3}m$)						
Y	4a	0	0	0	0.001	0.150
Dy	4a	0	0	0	0.001	0.150
Er	4a	0	0	0	0.001	0.150
Ho	4a	0	0	0	0.001	0.150
Yb	4a	0	0	0	0.001	0.150
Ta	4a	0	0	0	0.001	0.250
O	8c	0.250	0.250	0.250	0.031	0.872

* Oxygen vacancy concentration expressed as 1-occ.(O)

Table S4. Measured grain size, density, sound velocity, Grüneisen parameter γ, and Young's modulus E_0 RE_3TaO_7 specimens. Theoretical sound velocity, γ and E of RE_3TaO_7 were obtained by using the General Utility Lattice Program (GULP) package with the Buckingham potential.

Composition	Grain size (μm)	ρ_0 (g/cm3)	ρ (g/cm^3)	Relative density (%)	Sound velocity (m/s)		Grüneisen parameter γ		Young's modulus E (GPa)	
					Exp.	Cal.	Exp.	Cal.	Exp.	Cal.
1$RETaO_7$	2.95±0.24	9.63	9.42	97.8%	3762	3870	1.73	1.63	199	184
3$RETaO_7$	1.61±0.20	8.30	7.50	90.4%	3636	4133	1.60	1.56	197	203
4$RETaO_7$	2.40±0.18	8.51	8.16	95.9%	3770	3842	1.54	1.59	201	211
5$RETaO_7$	2.29±0.33	8.70	7.90	90.8%	3887	3884	1.71	1.60	234	215

3. Additional thermophysical properties

Thermophysical property measurement

The specific heat capacity (C_p) of RE_3TaO_7 ceramics measured by the DSC and calculated by the Neumann-Kopp rule at 300−1773 K is presented in Fig. S3 (A). For the family of RE_3TaO_7 ceramics, the C_p values calculated by the Neumann-Kopp rule are slightly lower than those measured by the DSC, but they show a similar variation tendency with increasing temperature. In this study, the C_p values calculated by Neumann-Kopp rule are used for subsequent calculation of κ. The thermal diffusivity (λ) of RE3TaO7 ceramics shows a temperature-independent at 300−1773 K, as shown in Fig. S3 (B).

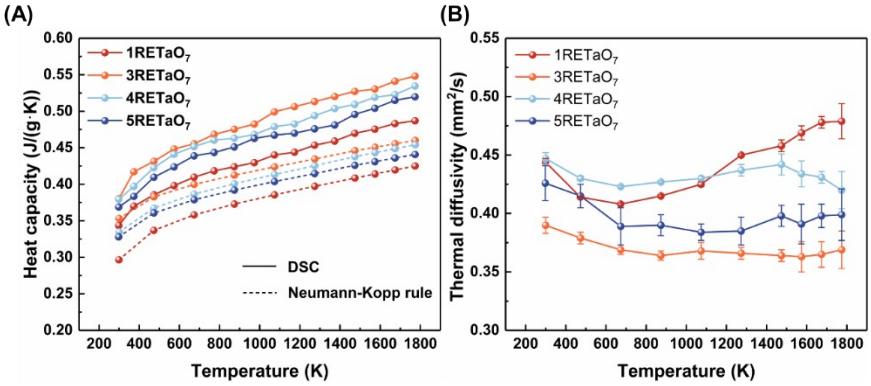

Fig. S3 (A) specific heat capacity properties (calculated by Neumann-Kopp (Dotted line) rule and differential scanning calorimetry (DSC) (Solid line)) and (B) thermal diffusion coefficients of RE_3TaO_7 ceramics.

4. Verification of molecular dynamics data

Before the calculation, the accuracy of force field and methodology used in this study was first verified. For the purpose, the calculated lattice constants and mechanical properties were compared with the experimental results respectively. It can be seen in Table S1 that the calculated lattice constants are in good agreement with the experimental values, and the relative errors are all less than 1%, indicating that the crystal structures of RE_3TaO_7 systems can be correctly described in this study. The Grüneisen parameter is an important thermophysical property to describe the anharmonic strength of phonon modes in solid materials. As shown in Table S4, the calculated γ is also in good agreement with the experimental values. In addition,

the mechanical properties related to heat transfer are also calculated. Again, the calculated Young's modulus are in good agreement with the experimental values. In conclusion, the excellent agreement between the calculated and experimental results confirms that the atomic models and the force field parameters adopted in this study are applicable to study the inherent heat transport in RE_3TaO_7 systems.

Having verified model and force field parameters, the intrinsic thermal conductivities of RE3TaO_7 were calculated using the EMD-GK method. To obtain accurate κ, the simulation time needs to be examined first. Taking 3RETaO_7 as an example, Figs. S4 (A) and S4 (B) show the variation in heat current autocorrelation function (HCACF) and κ as a function of the simulation correlation time, noting that the results here are averages after 10 independent calculations. It can be seen that the HCACF decays with the increase in the correlation time, while κ tends to converge, which is consistent with the fluctuation dissipation theory. Thus, the 20 ps correlation time used in this study is sufficient to obtain a converged κ. Subsequently, the effect of supercell size on was investigated as show in Fig. S4 (C), and it can be seen that the κ of supercell size was always oscillated near a certain value, which was consistent with the knowledge that the size effect could be eliminated in EMD-GK method. In summary, the supercell and the correlation time used in the calculation used in this study is reliable.

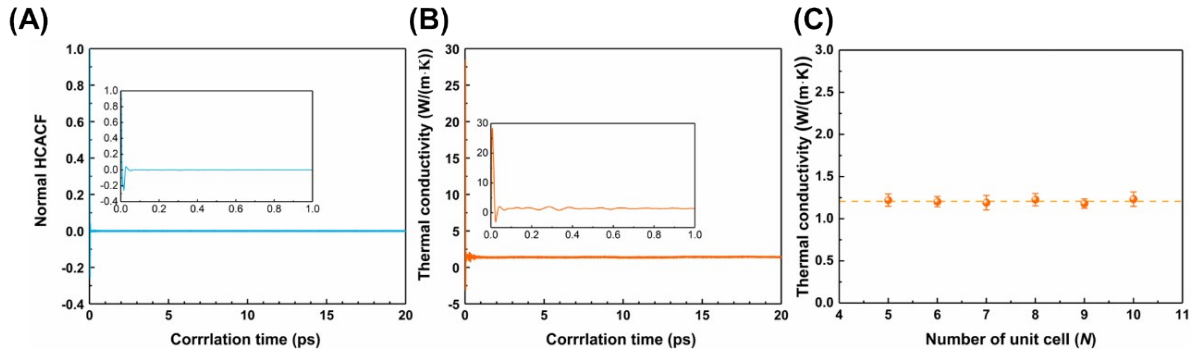

Fig. S4. Calculation of thermal conductivity: (A) Normal HCACF and (B) thermal conductivity as a function of the simulation time; (C) Thermal conductivity as a function of the supercell size (N×N×N).

5. Additional results from first-principles calculations

To consider the effect of spin polarization on the system, we plotted the equation of state (EOS) for spin polarization and non-spin polarization as shown in Fig. S5(A), and it can be found that the energy of the system with spin polarization is almost unchanged compared with that of non-spin polarization, and there is no net magnetic moment of the system. The band structure is shown in Fig. S5(B), and there is a band gap of 2.8749 eV in the system, indicating that the material is not metallic. Combining the lattice constants, EOS under spin polarization and non-spin polarization, and the band structure, it is concluded that the calculated parameters and pseudopotentials used are sufficiently accurate.

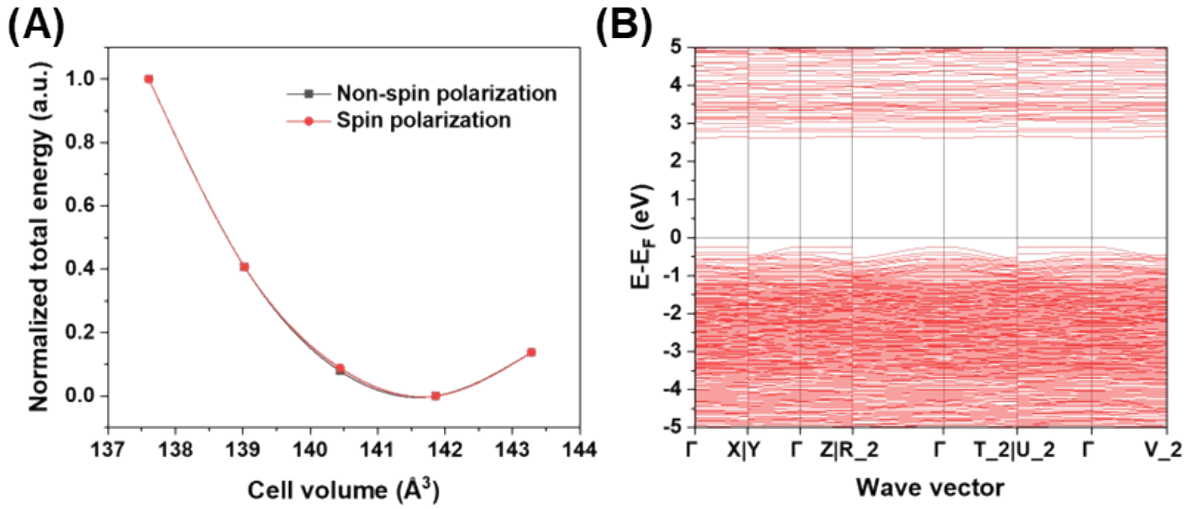

Fig. S5 (A) Equation of state for non-spin polarization and spin polarization, (B) the band structure of $5RETaO_7$.

Table S5 Calculated Atom-atom distance of $5RETaO_7$.

O atom	RE atom	Atom-atom distance, Å
O36	Dy1	2.27333
O42	Dy1	2.30598
O57	Dy1	2.27231
O64	Dy1	2.39864
O69	Dy1	2.25597
O76	Dy1	2.17042
O85	Dy1	2.16103

O38	Dy2	2.249
O45	Dy2	2.24732
O52	Dy2	2.57789
O59	Dy2	2.57326
O62	Dy2	2.35345
O69	Dy2	2.51424
O76	Dy2	2.18832
O83	Dy2	2.19003
O36	Dy3	2.32501
O43	Dy3	2.18107
O57	Dy3	2.31232
O67	Dy3	2.28354
O74	Dy3	2.51805
O81	Dy3	2.198
O88	Dy3	2.44385
O34	Dy4	2.41055
O43	Dy4	2.25931
O50	Dy4	2.59138
O55	Dy4	2.51207
O62	Dy4	2.37106
O71	Dy4	2.26592
O78	Dy4	2.24168
O83	Dy4	2.16955
O33	Dy5	2.34751
O37	Dy5	2.43837
O41	Dy5	2.25245
O48	Dy5	2.19463
O65	Dy5	2.19993
O72	Dy5	2.39731
O38	Y6	2.21587

O47	Y6	2.28279
O54	Y6	2.36411
O59	Y6	2.58174
O66	Y6	2.52117
O74	Y6	2.38794
O81	Y6	2.24861
O86	Y6	2.28648
O38	Y7	2.228
O45	Y7	2.19814
O51	Y7	2.23279
O58	Y7	2.51281
O65	Y7	2.64681
O72	Y7	2.60961
O79	Y7	2.33487
O86	Y7	2.36709
O44	Y8	2.58964
O51	Y8	2.18388
O58	Y8	2.38331
O61	Y8	2.29108
O68	Y8	2.25019
O75	Y8	2.17524
O82	Y8	2.34038
O34	Y9	2.26469
O43	Y9	2.25437
O49	Y9	2.31121
O53	Y9	2.63476
O65	Y9	2.31852
O81	Y9	2.17727
O86	Y9	2.2414
O39	Ho10	2.41595

O44	Ho10	2.19904
O51	Ho10	2.20412
O60	Ho10	2.24173
O72	Ho10	2.23295
O87	Ho10	2.24984
O40	Ho11	2.36774
O45	Ho11	2.26367
O51	Ho11	2.24016
O60	Ho11	2.60593
O63	Ho11	2.87606
O68	Ho11	2.33949
O76	Ho11	2.14394
O85	Ho11	2.2574
O35	Ho12	2.27828
O41	Ho12	2.28738
O57	Ho12	2.16475
O67	Ho12	2.3269
O73	Ho12	2.31435
O87	Ho12	2.24595
O33	Ho13	2.42241
O49	Ho13	2.26983
O61	Ho13	2.1035
O70	Ho13	2.35358
O77	Ho13	2.3742
O82	Ho13	2.24834
O33	Ho14	2.36608
O41	Ho14	2.43301
O55	Ho14	2.33267
O62	Ho14	2.25196
O69	Ho14	2.22419

O75	Ho14	2.31531
O82	Ho14	2.39097
O36	Yb15	2.2464
O43	Yb15	2.22134
O49	Yb15	2.32422
O56	Yb15	2.76663
O63	Yb15	2.25119
O78	Yb15	2.13361
O85	Yb15	2.14012
O38	Yb16	2.21517
O47	Yb16	2.15633
O58	Yb16	2.51563
O61	Yb16	2.31456
O70	Yb16	2.29138
O78	Yb16	2.14499
O83	Yb16	2.17517
O39	Yb17	2.56913
O46	Yb17	2.35732
O54	Yb17	2.24047
O67	Yb17	2.16285
O74	Yb17	2.26082
O80	Yb17	2.49371
O87	Yb17	2.29321
O35	Yb18	2.05307
O49	Yb18	2.23168
O53	Yb18	2.38222
O56	Yb18	2.16926
O80	Yb18	2.26083
O87	Yb18	2.2024
O34	Yb19	2.32173

O42	Yb19	2.41749
O48	Yb19	2.20718
O61	Yb19	2.20169
O68	Yb19	2.21474
O76	Yb19	2.11253
O83	Yb19	2.15288
O39	Ta20	2.25178
O60	Ta20	1.97971
O63	Ta20	1.88836
O70	Ta20	1.90869
O77	Ta20	2.09448
O84	Ta20	2.10622
O39	Ta21	2.15602
O52	Ta21	2.00771
O64	Ta21	1.93233
O69	Ta21	2.02833
O75	Ta21	1.94283
O84	Ta21	2.05162
O36	Ta22	1.98309
O42	Ta22	2.21611
O48	Ta22	2.06176
O56	Ta22	2.00571
O72	Ta22	2.11432
O79	Ta22	2.18246
O88	Ta22	2.01276
O37	Ta23	2.17615
O46	Ta23	1.95884
O53	Ta23	1.93003
O58	Ta23	1.92727
O65	Ta23	2.02442

O80	Ta23	2.19933
O37	Ta24	2.05736
O44	Ta24	1.88539
O52	Ta24	2.1881
O59	Ta24	1.94864
O66	Ta24	2.1692
O73	Ta24	1.91691
O46	Ta25	2.31914
O54	Ta25	2.03792
O59	Ta25	2.25106
O62	Ta25	1.9682
O71	Ta25	1.98765
O77	Ta25	2.09793
O82	Ta25	2.03726
O34	Ta26	1.92974
O42	Ta26	2.02429
O55	Ta26	2.01449
O66	Ta26	2.16777
O79	Ta26	2.03137
O86	Ta26	1.93766
O33	Ta27	2.20395
O37	Ta27	2.28091
O50	Ta27	1.88074
O55	Ta27	2.36302
O66	Ta27	2.11592
O74	Ta27	1.97231
O80	Ta27	2.02244
O35	Er28	2.5025
O41	Er28	2.28153
O48	Er28	2.50869

O56	Er28	2.31124
O63	Er28	2.24919
O68	Er28	2.19057
O75	Er28	2.71612
O84	Er28	2.28429
O40	Er29	2.15605
O45	Er29	2.12577
O52	Er29	2.45873
O67	Er29	2.26055
O73	Er29	2.49708
O79	Er29	2.29373
O88	Er29	2.34515
O35	Er30	2.17297
O50	Er30	2.28863
O57	Er30	2.20193
O64	Er30	2.31329
O71	Er30	2.26333
O77	Er30	2.29574
O84	Er30	2.28251
O40	Er31	2.17947
O47	Er31	2.1831
O54	Er31	2.4298
O64	Er31	2.33847
O71	Er31	2.23703
O78	Er31	2.22887
O85	Er31	2.18214
O40	Er32	2.18076
O47	Er32	2.09062
O53	Er32	2.32105
O60	Er32	2.30623

O81	Er32	2.1496
O88	Er32	2.24539

The force constants between various atoms decrease with the atom-atom distance is shown by Fig. S6. The variation pattern of force constants with atom-atom distance is consistent with that of -ICOHP. the force constants between O-Ta have higher force constants at shorter bond lengths, but decrease rapidly with increasing bond lengths, and overlap with those of O-RE in the range of 2.0 Å-2.4 Å, which reflects a degree of continuity characteristic of the force constant values within the crystal. The low force constants inside the crystal are basically contributed by O-RE, the average force constant of O-Ho is the lowest in the system, while the average force constants of O-Dy, O-Er, and O-Yb show a stepwise rise. The combined results of -ICOHP and force constants show that O-RE has the weakest bond within the system and that the bond strength varies between different rare earth ions and O. The covalency of O-Dy is the weakest among O-RE, while the energy potential change of O-Ho bond after deviation from the equilibrium scale is the smallest, which mirrors its weaker stiffness. The -ICOHP and force constants of O-Yb are the highest among O-RE, while O-Er lies in the middle.

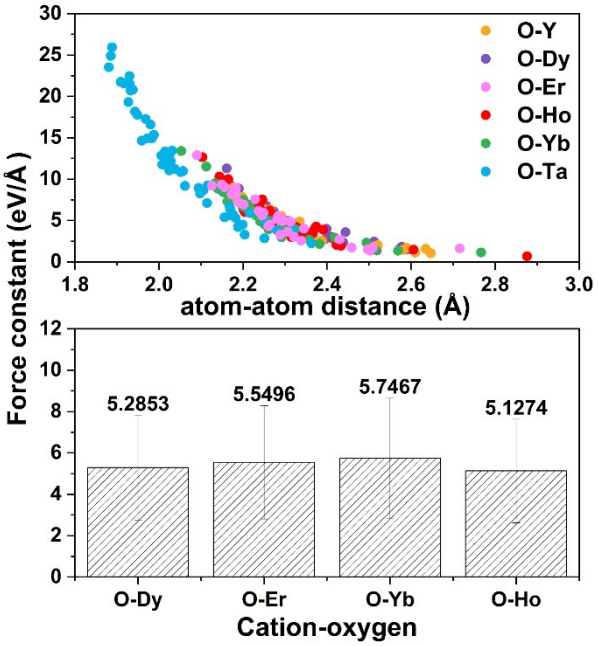

Fig. S6 The force constants between various atoms in $5RETaO_7$ as a function of atom-atom distance, and average value of force constant between O-Dy, O-Er, O-O-Yb, O-Ho.

6. Recognition of phonon vibration modes

According to the results in Fig. 3, the large gap between the κ obtained from BTE theory and the experimental results indicates that normal phonon transport under conventional picture cannot accurately describe the thermal conduction in defective fluorite tantalates. To illustrate the above issue, the phonon dispersion relationship with phonon linewidth in four different tantalate components was calculated using the phonon SED, as which based on classical MD can fully incorporate the complete lattice anharmonicity and allow for explicit treatment of disorder.

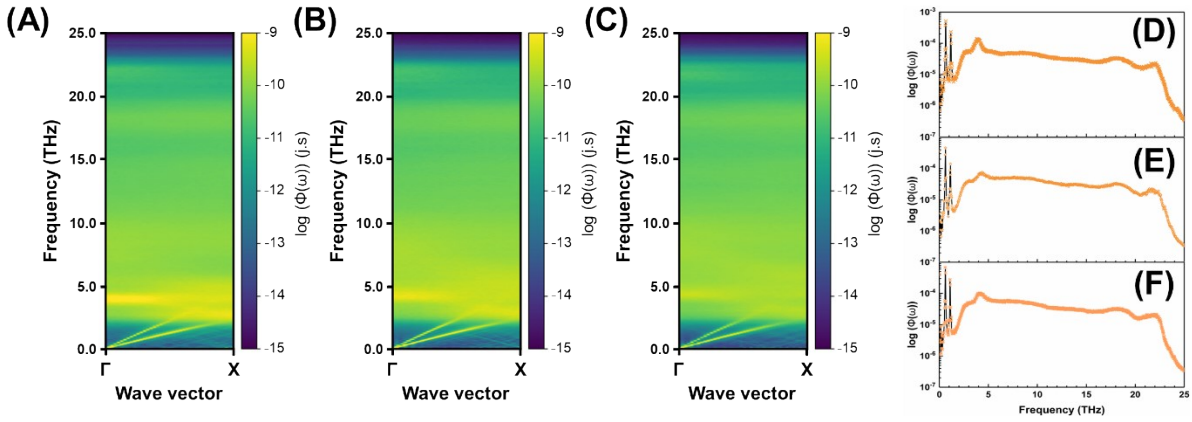

Fig. S7 Calculated SED for fluorite structures (A) $1RETaO_7$, (B) $3RETaO_7$, (C) $4RETaO_7$ at 300 K. (D)-(F) corresponds to their SED in the frequency domain at reduced wave vector q (0.125, 0.00, 0.00) respectively.

Actually, RE_3TaO_7 can be regarded as a substitutional compound where the trivalent RE^{3+} ions dope into the Ta_2O_5. To maintain the systems electro-neutrality, the substitution process is accompanied by the creation of oxygen vacancies. According to Kröger–Vink notation, the process of the RE_2O_3 alloying the Ta_2O_5 can be expressed as:

$$RE_2O_3 \xrightarrow{Ta_2O_5} 2RE''_{Ta} + 3O_o^{\times} + 2V_O^{\bullet\bullet}\backslash^* \text{ MERGEFORMAT (17)}$$

Clearly, the concentration of oxygen vacancies in RE_3TaO_7 is significantly greater than that of 7YSZ (~2%). High concentration of oxygen vacancies will strongly enhance the phonon scattering and affect the nature of phonons. It is known to all that phonon scattering rate is an important factor affecting phonon heat transfer, which can be described by Matthiessen's rule:

$$\frac{1}{\tau_{\text{total}(\lambda)}}=\frac{1}{\tau_{U(\lambda)}}+\frac{1}{\tau_{D(\lambda)}}+\frac{1}{\tau_{\Delta M(\lambda)}}+\frac{1}{\tau_{G(\lambda)}}+\frac{1}{\tau_{e-ph(\lambda)}} \quad \text{* MERGEFORMAT (18)}$$

where $\tau_{U(\lambda)}$, $\tau_{D(\lambda)}$, $\tau_{\Delta M(\lambda)}$, $\tau_{G(\lambda)}$, and $\tau_{e-ph(\lambda)}$ are phonon lifetimes due to the three-phonon Umklapp scattering, defect scattering, mass-difference scattering, grain boundary scattering, and electron-phonon scattering, respectively. The grain size of the sample in this study is about 2 μm (Table S4 and Fig S2). If the phonon MFP is much smaller than the grain size, the boundary scattering can also be ignored. spectral energy distribution (SED) of crystal lattice vibration could be calculated according to the molecular motion trajectory in MD simulation [111]. The phonon lifetime can be estimated from the SED. By Lorentz function fitting for SED with transverse acoustic branch mode about 0.6 THz, as shown in Fig. S8, the full width at half maximum (FWHM) of its vibration frequency is about 0.029 THz, then the corresponding phonon lifetime is 1.8×10^{-10} s, and the phonon MFP of is 684nm. This shows that even for low-frequency propagators, the mean free path is much smaller than the grain size, so boundary scattering can be ignored. Meanwhile, electron-phonon scattering is also ignored because rare earth tantalates are electronic insulating materials. Therefore, the above formula is simplified as:

$$\frac{1}{\tau_{\text{total}(\lambda)}}=\frac{1}{\tau_{U(\lambda)}}+\frac{1}{\tau_{D(\lambda)}}+\frac{1}{\tau_{\Delta M(\lambda)}} \quad \text{* MERGEFORMAT (19)}$$

The Umklapp scattering is given by Klemens expression [23,24]:

$$\frac{1}{\tau_{U(\lambda)}}=2\gamma^2\frac{K_B T}{SV_0}\frac{\omega^2}{\omega_D} \quad \text{* MERGEFORMAT (20)}$$

where S, V_0, and ω_D denote the share modules, volume per atom, and Debye frequency, respectively. The shear modulus is calculated by $S=E_0/(2+2\sigma)$. The vacancies are strong phonon scatterer because of missing mass and missing interatomic linkages. According to the perturbation theory, the vacancy-defect scattering can be expressed as [25]:

$$\frac{1}{\tau_{D(\lambda)}}=\frac{c\pi\omega_\lambda^2\text{DOS}(\omega_\lambda)}{4N}\left(\frac{\Delta M}{\overline{M}}\right)^2 \quad \text{* MERGEFORMAT (21)}$$

where c, N, and $\text{DOS}(\omega_\lambda)$ are defined as concentration of vacancy defects, number of atoms in the unit cell, and normalized phonon density of states, respectively. The DOS was obtained

by the Fourier transform of the calculated velocity autocorrelation function (VACF) in molecular dynamics simulation [26]:

$$\mathrm{DOS}(\omega)=\int_{-\infty}^{\infty}e^{i\omega t}\mathrm{VACF}(t)dt \quad \text{* MERGEFORMAT (22)}$$

Here, VACF(t) was given by the following:

$$\mathrm{VACF}(t)=\frac{1}{N}\sum_{i=1}^{N}\left\langle v_i(0)v_i(t)\right\rangle \quad \text{* MERGEFORMAT (23)}$$

where N is the number of atoms in the system, $v_i(t)$ is the velocity vector at time t in the microcanonical ensemble (NVE), and $\langle\ \rangle$ denotes the ensemble average. The effective value of $\frac{\Delta M}{\overline{M}}$ is defined as [27]:

$$\frac{\Delta M}{\overline{M}}=-\frac{M_{\mathrm{V}}}{\overline{M}}-2 \quad \text{* MERGEFORMAT (24)}$$

where $\overline{M}$ and M_{V} are the average mass per atom and mass of the defective atom, respectively. The term -2 represents the potential energy of the missing linkages. Mass-difference scattering is due to the difference in mass, which can be obtained from the following expression [24]:

$$\frac{1}{\tau_{M(\lambda)}}=\frac{V_0\Gamma\omega^4}{4\pi v_g^3} \quad \text{* MERGEFORMAT (25)}$$

where v_g is phonon group velocity. The Γ term is the measure of mass difference scattering intensity defined as:

$$\Gamma=\sum_i f_i\left(1-\frac{M_i}{\overline{M}}\right)^2 \quad \text{* MERGEFORMAT (26)}$$

Here f_i is the fraction concentration of the impurity atoms of mass M_i. Note that the total phonon lifetime ($\tau_{\mathrm{total}(\lambda)}$) was obtained by fitting the SED peak value with Lorentz function as follows [6]:

$$\phi(\mathbf{q},\omega_\lambda)=\frac{I}{1+\left[(\omega_\lambda-\omega_c)/\gamma\right]^2} \quad \text{* MERGEFORMAT (27)}$$

where I, ω_c, and γ denote the peak height of the SED, the frequency of the peak center, and the half width at half maximum of the peak, respectively. The $\tau_{\mathrm{total}(\lambda)}$ can be obtained from

$1/2\gamma$. It should be noted that the phonon eigenvectors were included in the SED calculation in this study, thus only peaks corresponding to specific modes can be found automatically.

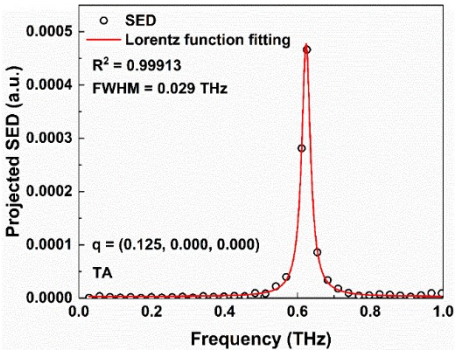

Fig. S8 5RETaO_7 SED distribution. The black circle is the result of SED, and the red solid line is the fitting curve of Lorentz function.

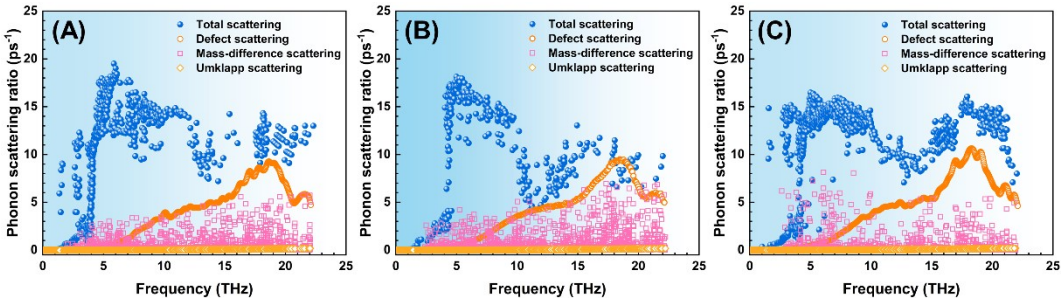

Fig. S9 Defect scattering rate, mass-difference scattering rate, Umklapp scattering rate, and total scattering rate in (A) 1RETaO_7, (B) 3RETaO_7, (C) 4RETaO_7.

To directly understand the effect of this inhomogeneous interatomic bonding on phonon modes, phonon dispersion relationships in one-dimensional (1D) diatomic chains in the first Brillouin zone containing mass difference and interatomic bond energy difference were calculated, as shown in Figs. S10 (A) and (B).

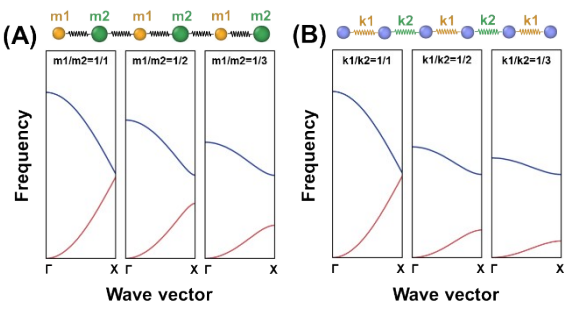

Fig. S10 The phonon dispersion relationship of one-dimensional diatomic chain in the first Brillouin zone with (A) different mass and (B) different interatomic binding.

Recognition of phonon vibration modes

To intuitively understand these modes, the phonon eigenvectors is normalized into a unit sphere of polarization [28]:

$$\varepsilon_{i,\lambda} = \frac{\mathbf{e}_{i\alpha,\lambda}}{\sum_{\alpha}\left(\mathbf{e}^{*}_{i\alpha,\lambda}\cdot\mathbf{e}_{i\alpha,\lambda}\right)} \qquad \backslash* \text{ MERGEFORMAT (28)}$$

where $\mathbf{e}_{i\alpha,\lambda}$ is the eigenvector of atom i along the α direction, and the superscript '*' represents the complex conjugate transpose of $\mathbf{e}_{i\alpha,\lambda}$. Each normalized eigenvector is plotted as a point on the polarization sphere, as shown in Fig. S11.

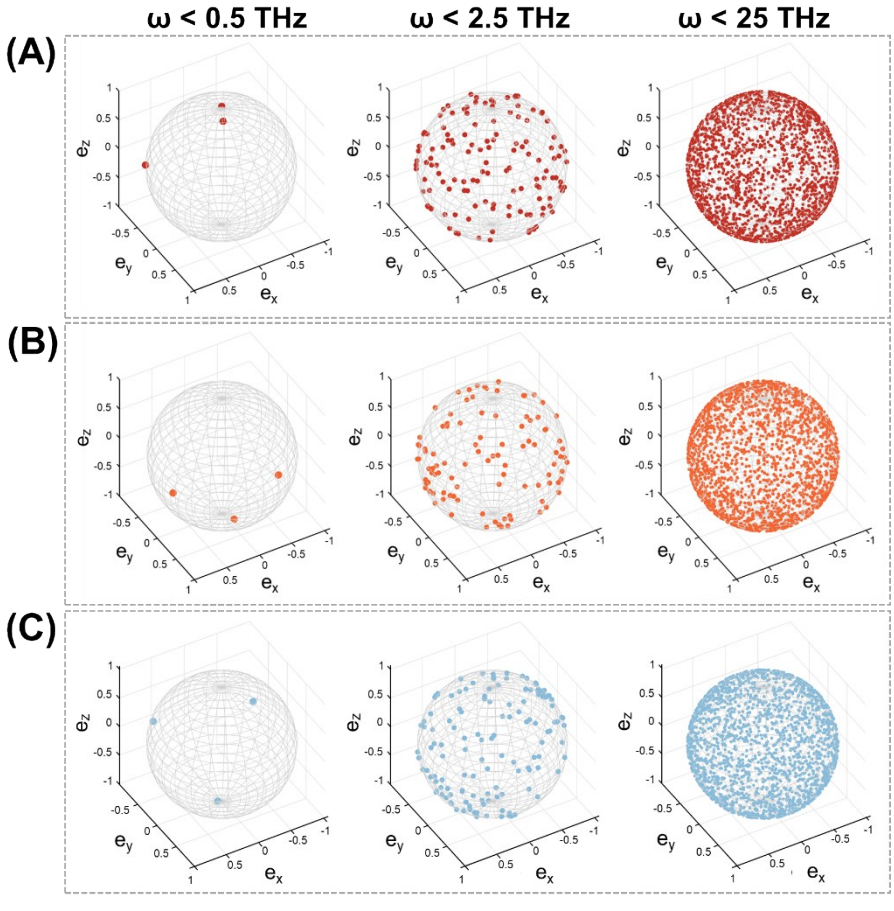

Fig. S11 Polarization of phonon modes of (A) 1RETaO$_7$, (B) 3RETaO$_7$, (C) 4RETaO$_7$ in frequency domains below 0.5 THz, 2.5 THz, and 25 THz.

The localized mode of phonons can be identified using phonon participation ratio (PR) [29]:

$$\mathrm{PR}_\lambda = \frac{\left(\sum_i \mathbf{e}^*_{i\alpha,\lambda} \cdot \mathbf{e}_{i\alpha,\lambda}\right)^2}{N\sum_i \left(\mathbf{e}^*_{i\alpha,\lambda} \cdot \mathbf{e}_{i\alpha,\lambda}\right)^2} \qquad \text{* MERGEFORMAT (29)}$$

where N is the total of atoms. If all atoms in the simulation system contribute to a given phonon modes, the value of PR approaches 1. Conversely, if a small fraction of atoms is associated with a given mode, the mode is characterized to be localized (i.e., locons), and the corresponding PR value less than 0.1. As shown in Fig. S12, the majority of phonon modes in defective fluorite tantalate structures have moderate PR values between 0.1 and 0.5, indicating that most phonons are delocalized. However, some phonon modes at high frequencies are localized, which is associated with phonon scattering by oxygen vacancies and mass differences. Also, such localized modes have no contribution to thermal conduction. To further investigate which atomic species are involved in specific vibration modes, the total PR were projected onto different atomic species:

$$\mathrm{PR}_{g,\lambda} = \mathrm{PR}_\lambda \left(\sum_{i\in g} \mathbf{e}^*_{i\alpha,\lambda} \cdot \mathbf{e}_{i\alpha,\lambda} \right)^2 \qquad \text{* MERGEFORMAT (30)}$$

As shown in Fig. S12 (A), phonon modes with frequencies below 6 THz in 1RETaO$_7$ are mainly driven by the vibration of the Yb atom, while the remaining phonon modes is primarily attributed to the vibration of the O atom. Moreover, the vibration of the Ta atom in the entire phonon spectrum is localized.

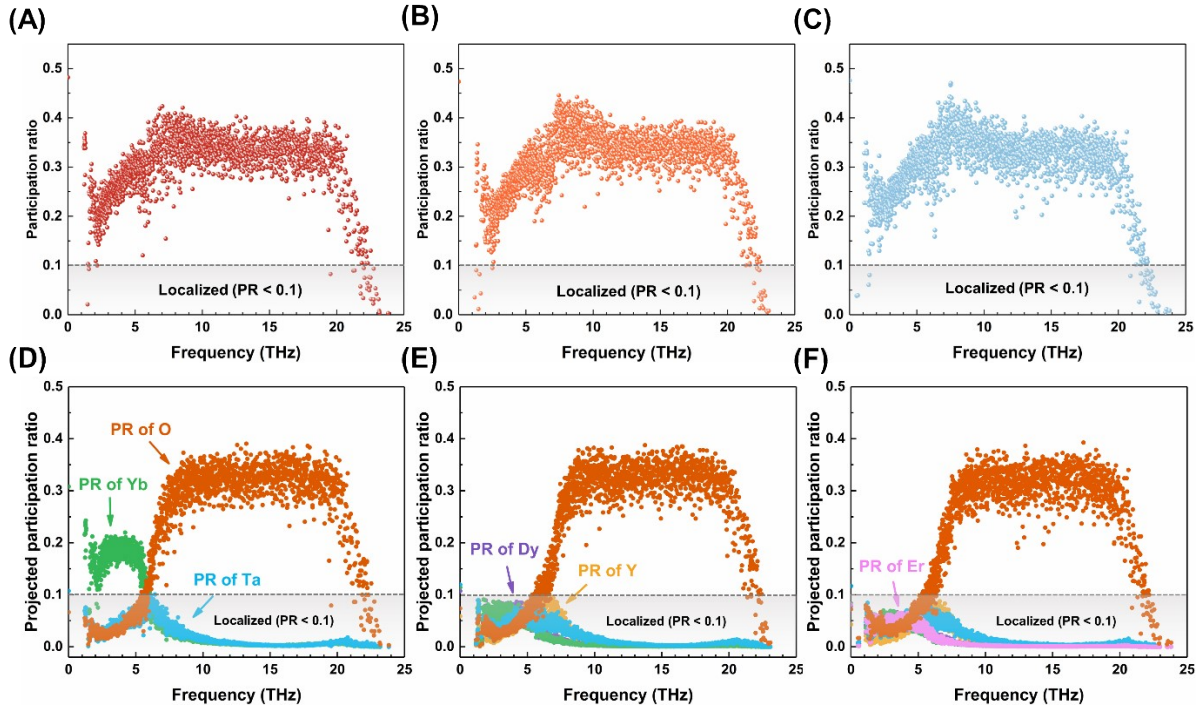

Fig. S12 Total phonon participation ratio for (A) $RETaO_7$, (B) $3RETaO_7$, and (C) $4RETaO_7$. (D)-(F) represent projected participation ratio of the different atomic species.

The eigenvector periodicity (EP) parameter, developed by Seyf and Henry [30], measures the periodicity of an arbitrary mode compared to completely wavelike modes, enabling the differentiation between propagons and diffusons:

$$\mathrm{EP}_{\lambda}=\frac{\left|\sum_{i}\sum_{j\geq 1}\left(\mathbf{e}_{i,\lambda}^{*}\cdot\mathbf{e}_{i,\lambda}\right)\left(f\left(\mathbf{q}\cdot\mathbf{r}_{i}+\varphi\right)f\left(\mathbf{q}\cdot\mathbf{r}_{j}+\varphi\right)\right)\right|}{\left|\sum_{i}\sum_{j\geq 1}\left(\mathbf{s}_{i,\lambda}^{*}\cdot\mathbf{s}_{i,\lambda}\right)\left(f\left(\mathbf{q}\cdot\mathbf{r}_{io}+\varphi\right)f\left(\mathbf{q}\cdot\mathbf{r}_{jo}+\varphi\right)\right)\right|}\ \backslash^{*}\ \mathrm{MERGEFORMAT} \quad (31)$$

where $\mathbf{s}_{i,\lambda}$ denotes the eigenvector of the fictitious mode, $\mathbf{r}_{i(j)}$ denotes the position of the *i*-th (*j*-th) atom in the mode λ, and the subscript index *o* denotes the equilibrium position. Function *f* is the periodic function chosen for comparison. It is noted that any spatially oscillating function, such as $\sin\left(\mathbf{q}\cdot\mathbf{r}_{io}+\varphi\right)$, $\cos\left(\mathbf{q}\cdot\mathbf{r}_{io}+\varphi\right)$, etc. will get the same results after properly normalization. In the study, $\cos\left(\mathbf{q}\cdot\mathbf{r}_{io}+\varphi\right)$ was used to calculate EP. Generally, if a mode has an EP > 0.2, it can be considered a propagon. The boundary that distinguishes between propagons and diffusions is typically known as the Ioffe-Regel transition (IRT). As illustrated

in Fig. S13, only a limited number of modes below 1.7 THz can be considered propagons, which is consistent with the SED analysis. It can also be observed that the IRT value does not decrease significantly after high entropy. However, for diffusons (EP < 0.2), the EP value decreases with the enhancement of the high entropy effect and the phonon modes exhibit a strong randomness, which is consistent with the present findings.

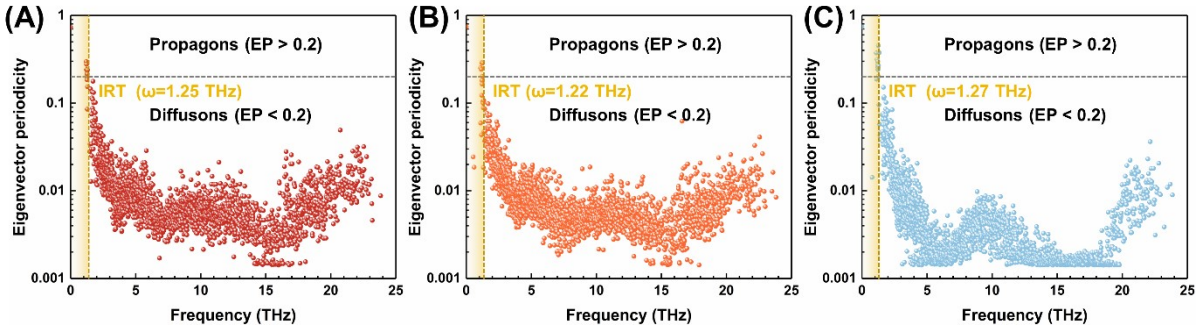

Fig. S13 Eigenvector periodicity of the phonon modes in (A) $1RETaO_7$, (B) $3RETaO_7$, and (C) $4RETaO_7$.

7. Multimodal phonon thermal transport

The propagons-contributed thermal conductivity (κ_P) can be determined using the phonon BTE, while the diffusons-contributed thermal conductivity (κ_D) can be described using the Allen-Feldman (A-F) diffusion theory [31]:

$$\kappa_D = \frac{1}{V}\sum\nolimits_{\lambda} C_\lambda D_\lambda \qquad \backslash* \text{ MERGEFORMAT (32)}$$

where C_λ and D_λ are specific heat capacity and diffusivity of phonon mode λ. The sum is evaluated over all diffusons belonging to the Ioffe–Regel regime. D_λ was defined as:

$$D_\lambda = \frac{\pi V^2}{3\mathrm{h}^2\omega_\lambda^2}\sum_{\lambda_1}^{\lambda\neq\lambda_1}\left|\mathbf{S}_{\lambda\lambda_1}\right|^2\delta\left(\omega_\lambda-\omega_{\lambda_1}\right) \backslash* \text{ MERGEFORMAT (33)}$$

where $\mathbf{S}_{\lambda\lambda_1}$ is the off-diagonal term of the heat-current operator calculated from the LD theory, δ is the Dirac function. As shown in Fig.S14, the contribution of the propagons in $1RETaO_7$, $3RETaO_7$, $4RETaO_7$ and $5RETaO_7$ to the overall κ is 31.5%, 22%, 17.7% and 9.4%, respectively.

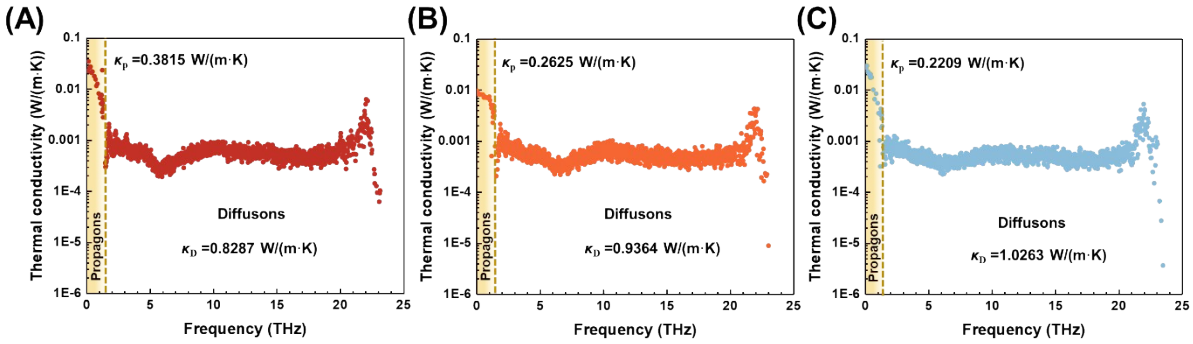

Fig. S14 Mode decomposition of the thermal conduction for (A) 1RETaO7, (B) 3RETaO7, and (C) 4RETaO7 at 300K

Multimodal phonon transport at different temperatures was investigated, as shown in Fig. S15.

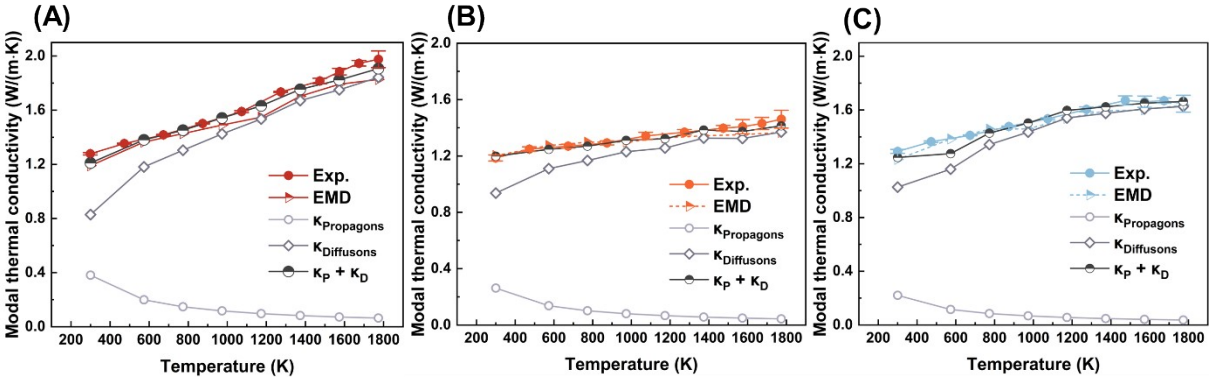

Fig. S15 Temperature dependent modal thermal conductivity for (A) $1RETaO_7$, (B) $3RETaO_7$, (C) $4RETaO_7$.

References

1. S. Plimpton. Fast Parallel Algorithms for Short-Range Molecular Dynamics. *J. Comput. Phys.* **117**, 1-19 (1995).
2. N. Metropolis, A.W. Rosenbluth, M.N. Rosenbluth, A.H. Teller and E. Teller. Equation of State Calculations by Fast Computing Machines. *J. Chem. Phys* **21**, 1087-1092 (1953).
3. S. Chen, Z.H. Aitken, S. Pattamatta, Z. Wu, Z.G. Yu, D.J. Srolovitz, P.K. Liaw and Y.W. Zhang. Simultaneously enhancing the ultimate strength and ductility of high-entropy alloys via short-range ordering. *Nat. Commun.* **12**, 4953 (2021).
4. P.K. Schelling, S.R. Phillpot and P. Keblinski. Comparison of atomic-level simulation methods for computing thermal conductivity. *Phys. Rev. B* **65**, 144306 (2002).
5. D. Surblys, H. Matsubara, G. Kikugawa and T. Ohara. Application of atomic stress to compute heat flux via molecular dynamics for systems with many-body interactions. *Physical review. E* **99**, 051301 (2019).
6. J.A. Thomas, J.E. Turney, R.M. Iutzi, C.H. Amon and A.J.H. McGaughey. Predicting phonon dispersion relations and lifetimes from the spectral energy density. *Phys. Rev. B* **81**, 081411 (2010).
7. T. Tadano, Y. Gohda and S. Tsuneyuki. Anharmonic force constants extracted from first-principles molecular dynamics: applications to heat transfer simulations. *J. Phys. Condens. Matter* **26**, 225402 (2014).
8. X. Wu, J. Walter, T. Feng, J. Zhu, H. Zheng, J.F. Mitchell, N. Biškup, M. Varela, X. Ruan, C. Leighton and X. Wang. Thermal Conductivity: Glass-Like Through-Plane Thermal Conductivity Induced by Oxygen Vacancies in Nanoscale Epitaxial $La_{0.5}Sr_{0.5}CoO_{3-\delta}$. *Adv. Funct. Mater.* **27**, 1770284 (2017).
9. R. Dronskowski and P.E. Bloechl. Crystal orbital Hamilton populations (COHP): energy-resolved visualization of chemical bonding in solids based on density-functional calculations. *J. Phys. Chem.* **97**, 8617-8624 (1993).
10. V.L. Deringer, A.L. Tchougréeff and R. Dronskowski. Crystal Orbital Hamilton Population (COHP) Analysis As Projected from Plane-Wave Basis Sets. *J. Phys. Chem. A* **115**, 5461-5466 (2011).

11. M. Küpers, P.M. Konze, S. Maintz, S. Steinberg, A.M. Mio, O. Cojocaru-Mirédin, M. Zhu, M. Müller, M. Luysberg, J. Mayer, M. Wuttig and R. Dronskowski. Inside Back Cover: Unexpected Ge–Ge Contacts in the Two-Dimensional Ge_4Se_3Te Phase and Analysis of Their Chemical Cause with the Density of Energy (DOE) Function (Angew. Chem. Int. Ed. 34/2017). *Angew. Chem. Int. Ed.* **56**, 10247-10247 (2017).
12. S. Maintz, V.L. Deringer, A.L. Tchougréeff and R. Dronskowski. LOBSTER: A tool to extract chemical bonding from plane-wave based DFT. *J Comput. Chem.* **37**, 1030-1035 (2016).
13. S. Baroni, S. de Gironcoli, A. Dal Corso and P. Giannozzi. Phonons and related crystal properties from density-functional perturbation theory. *Rev. Mod. Phys.* **73**, 515-562 (2001).
14. A. Togo and I. Tanaka. First principles phonon calculations in materials science. *Scripta Mater.* **108**, 1-5 (2015).
15. M. Khazaei, J. Wang, M. Estili, A. Ranjbar, S. Suehara, M. Arai, K. Esfarjani and S. Yunoki. Novel MAB phases and insights into their exfoliation into 2D MBenes. *Nanoscale* **11**, 11305-11314 (2019).
16. S. Maintz, V.L. Deringer, A.L. Tchougréeff and R. Dronskowski. Analytic projection from plane-wave and PAW wavefunctions and application to chemical-bonding analysis in solids. *J. Comput. Chem.* **34**, 2557-2567 (2013).
17. Y. Liu, K.T. Eddie Chua, T.C. Sum and C.K. Gan. First-principles study of the lattice dynamics of Sb_2S_3. *Phys. Chem. Chem. Phys.* **16**, 345-350 (2014).
18. V.L. Deringer, R.P. Stoffel, M. Wuttig and R. Dronskowski. Vibrational properties and bonding nature of Sb2Se3 and their implications for chalcogenide materials. *Chem. Sci.* **6**, 5255-5262 (2015).
19. L. Wang, X. Zhou, T. Ma, D. Liu, L. Gao, X. Li, J. Zhang, Y. Hu, H. Wang, Y. Dai and J. Luo. Superlubricity of a graphene/MoS_2 heterostructure: a combined experimental and DFT study. *Nanoscale* **9**, 10846-10853 (2017).
20. M. Pirzada. Oxygen migration in $A_2B_2O_7$ pyrochlores. *Solid State Ionics* **140**, 201-208 (2001).
21. L. Minervini, R.W. Grimes and K.E. Sickafus. Disorder in Pyrochlore Oxides. *Journal*

of the American Ceramic Society **83**, 1873-1878 (2004).

22. M.R. Levy, R.W. Grimes and K.E. Sickafus. Disorder processes in $A^{3+}B^{3+}O_3$compounds: implications for radiation tolerance. *Philosophical Magazine* **84**, 533-545 (2004).
23. A. Balandin and K.L. Wang. Significant decrease of the lattice thermal conductivity due to phonon confinement in a free-standing semiconductor quantum well. *Phys. Rev. B* **58**, 1544-1549 (1998).
24. J. Zou and A. Balandin. Phonon heat conduction in a semiconductor nanowire. *J. Appl. Phys.* **89**, 2932-2938 (2001).
25. P.G. Klemens and D.F. Pedraza. Thermal conductivity of graphite in the basal plane. *Carbon* **32**, 735-741 (1994).
26. J.M. Dickey and A. Paskin. Computer Simulation of the Lattice Dynamics of Solids. *Phys. Rev.* **188**, 1407-1418 (1969).
27. P.G. Klemens. Phonon scattering by oxygen vacancies in ceramics. *Physica B Condens. Matter* **263-264**, 102-104 (1999).
28. P.K. Schelling and S.R. Phillpot. Mechanism of Thermal Transport in Zirconia and Yttria-Stabilized Zirconia by Molecular-Dynamics Simulation. *J. Am. Ceram. Soc.* **84**, 2997-3007 (2001).
29. R. Biswas, A.M. Bouchard, W.A. Kamitakahara, G.S. Grest and C.M. Soukoulis. Vibrational Localization in Amorphous Silicon. *Phys. Rev. Lett.* **60**, 2280-2283 (1988).
30. H.R. Seyf and A. Henry. A method for distinguishing between propagons, diffusions, and locons. *J. Appl. Phys.* **120** (2016).
31. P.B. Allen and J.L. Feldman. Thermal conductivity of disordered harmonic solids. *Phys. Rev. B* **48**, 12581-12588 (1993).